Band-gap and sub-band-gap photoelectrochemical processes at nanocrystalline CdS grown on ZnO by successive ionic layer adsorption and reaction method

8 AUTHORS, INCLUDING:

Alexander Mazanik
Belarusian State University
56 PUBLICATIONS **106** CITATIONS

SEE PROFILE

Anatoly Kulak
Institute of General and Inorganic Chemistry,…
107 PUBLICATIONS **772** CITATIONS

SEE PROFILE

S.K. Poznyak
Belarusian State University
68 PUBLICATIONS **1,416** CITATIONS

SEE PROFILE

Oleksandr L. Stroyuk
National Academy of Sciences of Ukraine
141 PUBLICATIONS **822** CITATIONS

SEE PROFILE

Accepted Manuscript

Band-gap and sub-band-gap photoelectrochemical processes at nanocrystalline CdS grown on ZnO by successive ionic layer adsorption and reaction method

M.V. Malashchonak, .. Streltsov, A.V. Mazanik, A.I. Kulak, S.K. Poznyak, O.L. Stroyuk, S.Ya. Kuchmiy, P.I. Gaiduk

Please cite this article as: M.V. Malashchonak, .. Streltsov, A.V. Mazanik, A.I. Kulak, S.K. Poznyak, O.L. Stroyuk, S.Ya. Kuchmiy, P.I. Gaiduk, Band-gap and sub-band-gap photoelectrochemical processes at nanocrystalline CdS grown on ZnO by successive ionic layer adsorption and reaction method, *Thin Solid Films* (2015), doi: 10.1016/j.tsf.2015.04.057

Band-gap and sub-band-gap photoelectrochemical processes at nanocrystalline CdS grown on ZnO by successive ionic layer adsorption and reaction method

M.V. Malashchonak[*1], E.A. Streltsov[1], A.V. Mazanik[1], A.I. Kulak[2], S.K. Poznyak[1], O.L. Stroyuk[3], S.Ya. Kuchmiy[3], P.I. Gaiduk[1]

[1]Belarusian State University, Nezalezhnastsi Av. 4, Minsk 220030, Belarus, *e-mail*: streltea@bsu.by

[2]Institute of General and Inorganic Chemistry, National Academy of Sciences of Belarus, Surganova str., 9/1, Minsk 220072, Belarus, *e-mail*: kulak@igic.bas-net.by

[3]L.V. Pysarzhevsky Institute of Physical Chemistry of National Academy of Sciences of Ukraine, 31 prosp. Nauky, 03028, Kyiv, Ukraine, *e-mail*: stroyuk@inphyschem-nas.kiev.ua

Abstract

Cadmium sulfide nanoparticles (NPs) deposition by the successive ionic layer adsorption and reaction (SILAR) method on the surface of mesoporous ZnO micro-platelets with a large specific surface area (110 ± 10 m^{2}g^{-1}) results in formation of ZnO/CdS heterostructures exhibiting a high incident photon-to-current conversion efficiency (Y) not only within the region of CdS fundamental absorption ($Y_{max} = 90$ %; 0.1 M Na$_2$S + 0.1 M Na$_2$SO$_3$), but also in the sub-band-gap (SBG) range ($Y_{max} = 25$ %). The onset potentials of SBG photoelectrochemical processes are more positive than the band-gap (BG) onset potential by up to 100 mV. A maximum incident photon-to-

---

[*] Corresponding author. Tel./fax: +375 17 2095387
E-mail address: che.malasche@gmail.com

current conversion efficiency value for SBG processes is observed at larger amount of deposited CdS in comparison with the case of BG ones. The Urbach energy (E_U) of CdS NPs determined from the photocurrent spectra reaches a maximal value on an early deposition stage ($E_U = 93$ mV at SILAR cycle number $N = 5$), then lowers somewhat ($E_U = 73$ mV at $N = 10$) and remains steady in the range of N from 20 to 300 ($E_U = 67 \pm 1$ mV). High efficiency of the photoelectrochemical SBG processes are interpreted in terms of light scattering in the ZnO/CdS heterostructures.

Key words: CdS; ZnO; SILAR; Sub-band-gap processes; Photoelectrochemistry.

Highlights

ZnO/CdS films demonstrate high quantum efficiency (25%) for sub-band-gap transitions.

Onset photocurrent potentials for sub-band-gap processes differ than those for band-gap ones.

Sub-band-gap transitions are caused by band-tail states in CdS nanoparticles.

2

1. Introduction

Deposition of nanometer-scale layers of metal chalcogenides by the successive ionic layer adsorption and reaction (or SILAR) technique is a convenient and commonly used method of producing electrodes for quantum-dot-sensitized solar cells (QDSSCs). SILAR can be applied to deposit metal sulfides (CdS, ZnS, PbS, Bi_2S_3, In_2S_3, Sb_2S_3, Cu_xS, etc.) [1−5], selenides (PbSe [6, 7], CdSe [5, 8−10]), and tellurides (CdTe [5, 11]). A metal chalcogenide layer is formed by immersion of a substrate into solution of a metal salt (nitrate, acetate, sulfate, etc.) followed by rinsing with a solvent (water, alcohol) and immersion into solution of sodium sulfide (Na_2S), Na_2SeSO_3, or Se(IV) and Te(IV) compounds in the presence of a strong reducing agent. The thickness of a chalcogenide layer is incremented by repetitions of the SILAR procedure for a desired number N of cycles. Such method is attractive from the viewpoint of simplicity, low cost, easy control of the amount of deposited metal chalcogenide (by varying the N), as well as tailoring the optical and electrophysical properties of the deposit changing the concentration, temperature and pH of the metal and chalcogene source solutions.

The band gap E_g of a semiconductor-sensitizer is a crucial parameter affecting the light conversion efficiency in QDSSCs. In some reports (see, for example, refs. 12–14 and references therein) the SILAR method was found to produce CdS deposits with a lower bandgap as compared to that of the products obtained by other deposition techniques. A detailed analysis of the pronounced "red" E_g shift (up to 10%) of the CdS films produced by SILAR on the surface of zinc oxide with the cycle number N increasing up to 100−200 was reported in [13]. It was argued [13] that the red shift is not due to a change in bandgap of the CdS layer but rather to a pronounced sub-bandgap tailing, which is amplified by the high surface area in the composite film. Another possible interpretations of the band gap shrinkage were also discussed in [13], such as electron transitions between the CdS valence band and the ZnO conduction band, surface absorption and hybridization of Cd−Cd bonds between adjacent NPs.

In our previous work we have shown that the CdS nanoparticles deposited at a SILAR cycle number (N) from 5 to 10 exhibit a broadening of the band gap by 0.17–0.31 eV as compared with that of the CdS particles grown at $N = 30$ [14]. The photocurrent spectroscopy of ZnO/CdS heterostructures have shown that the band gap of CdS NPs deposited at $N > 20$ is smaller by ~0.08 eV than that of bulk cadmium sulfide. It was concluded that this effect is not associated with photoexcitation of structural defects but rather reflects intrinsic electronic properties of SILAR-deposited CdS nanoparticles.

The present paper is aimed at further understanding of the origins of red shift in the photocurrent spectra of ZnO/CdS heterostructures with an increase of the cycle number N of the SILAR deposition of cadmium sulfide NPs onto the ZnO platelets. A special focus is made on distinction of the contributions of band-gap (BG) and sub-band-gap (SBG) photoelectrochemical processes into the photoactivity of ZnO/CdS heterostructures with different N. Particularly the photocurrent onset-potentials for BG and SBG photoelectrochemical processes as well as IPCE and Urbach energy dependencies on the CdS SILAR deposition cycle number are revealed.

2. Experimental

ZnO coatings were electrodeposited on the surface of FTO plates. In a typical procedure, the plate was immersed into ethanol-water (50/50 v/v) solution containing 0.1 mol dm^{-3} Zn(NO$_3$)$_2$, 0.1 mol dm^{-3} KCl and 4 g dm^{-3} polyvinylpyrrolidone (with a molecular mass of 40000 g/mol). Deposition was carried out at a constant E vs. Ag/AgCl/KCl (sat.) = −1000 mV and 50 ^{o}C for 25 min. A Pt wire served as a counter electrode. The electrolysis of water-ethanol solutions of zinc(II) nitrate results in deposition of a layer of zinc(II) hydroxychloride Zn$_5$(OH)$_8$Cl$_2$ [14, 15]. Subsequently, the electrodeposited films were calcined at 360 ^{o}C in air for 1 h to obtain ZnO crystalline mesoporous films.

CdS nanoparticles were deposited onto the ZnO films by the SILAR technique. In a typical procedure, the ZnO film was dipped into 0.1 mol dm^{-3} Cd(NO$_3$)$_2$ aqueous solution for 10 s under

4

vigorous stirring, retracted and rinsed with distilled water, then dipped for another 10 s into 0.01 mol dm^{-3} Na$_2$S aqueous solution under vigorous stirring, retracted and rinsed again with distilled water. The deposition cycles were repeated 5 – 300 times. Finally the sample was thoroughly rinsed with distilled water and air dried.

Photoelectrochemical measurements were carried out in a standard two-compartment three-electrode cell involving a platinum counter-electrode and an Ag/AgCl/KCl (sat.) electrode as the reference electrode (+0.201 V vs. SHE). Aqueous solution containing 0.1 M Na$_2$S and 0.1 M Na$_2$SO$_3$ with pH 12.3 acted as electrolyte for photoelectrochemical measurements. The cell was controlled by a conventional potentiostat Elins P8 (Russia). Photocurrent–potential curves and photocurrent action spectra were obtained using a set-up equipped with a high-intensity grating monochromator, a 1 kW xenon lamp and a slowly rotating light chopper (0.3 Hz). Spectral dependences of the photocurrent and light intensity distribution at the monochromator output were used to calculate the incident photon-to-current conversion efficiency (Y).

Raman spectra were registered at room temperature using a confocal Nanofinder HE (LOTIS TII, Belarus – Japan) spectrometer. Solid-state laser emitting at 473 nm ($h\nu$ = 2.62 eV) was used for excitation of the samples. Scattered light without analysis of its polarization was dispersed on a diffraction grating with 1800 lines per mm with the spectral resolution not lower than 1 cm^{-1} and detected using a thermostated CCD camera with a signal acquisition time of 120 s. Calibration was performed using a built-in gas-discharge lamp with an accuracy better than 1 cm^{-1}.

X-ray diffraction analysis was performed on a Bruker D8 Advance diffractometer (copper K_α irradiation, λ = 0.1540 nm) in a range of $2\theta = 10° - 90°$ and a scanning rate of 1 grade per min.

Crystallinity, phase composition and morphology of samples were analyzed by transmission electron microscopy (TEM) and selected-area electron diffraction (SAED) in plan-view geometry using a Philips CM20 instrument operating at 200 kV. Prior to TEM measurements the prepared films were carefully scraped, ultrasonically dispersed in distilled water and transferred to copper grids covered with a collodion film.

Absorption isotherms were obtained with N_2 at 77 K by using an ASAP 2020 (Micromeritics, USA) analyzer. The surface area was calculated from a linear part of the Brunauer–Emmett–Teller (BET) plot. The pore size distribution was estimated using the Barret–Joyner–Halenda (BJH) model with the Halsey equation [16] for mesopores including those with the size bordering with microrange and the Horvath-Kawazoe (HK) method for mesopores with the size close to the nanorange.

3. Results and discussion

3.1. Structural characterization of ZnO and ZnO/CdS coatings.

The electrodeposited ZnO films with an average thickness of 2 μm as determined from the cross-sectional SEM views were used as a wide-gap substrate for CdS deposition by SILAR. Fig. 1 shows that the zinc oxide films are formed by micro-platelets with a lateral size of 0.5−1.5 μm and a thickness of 100–200 nm. The micro-platelets are porous and formed by finest ZnO particles with a size of several tens of nanometers (Fig. 1b). SEM studies show (Fig. 1c) that deposition of CdS by SILAR even after 300 repetitions does not influence the macroscale structure of the film notably.

Developed porous structure of the electrodeposited ZnO films imparts them a high specific surface area. The N_2 absorption/desorption isotherm (Fig. 2a) exhibits a typical IV-type shape accompanied by a H3-type hysteresis loop (accordingly to the IUPAC classification). This fact can be attributed to the dominance of mesopores formed by aggregation of ZnO NPs giving rise to slit-shaped pores [17]. The surface area calculated from a linear section of the BET plot for the electrodeposited ZnO coating was found to be 105 ± 12 $m^2\,g^{-1}$, which is close to the BJH desorption cumulative surface area, 117 ± 9 $m^2\,g^{-1}$, for pores between 2 nm and 300 nm in diameter. The pore size distribution determined from the desorption branch of N_2 isotherm by the BJH method confirms the dominance of mesopores in the ZnO coatings (Fig. 2c). The pore size distribution encompasses the range of 15–90 nm with a peak at 35−36 nm. A minor peak around 4 nm for the

ZnO/CdS sample can be attributed to the tensile strength effect with no relation to the mesoporosity [18].

Along with the large mesopores, the Horvath-Kawazoe plot shows the presence of smaller 2−3-nm pores (Fig. 2b) that are apparently responsible for a micropore area of 12.4 m^2 g^{-1} derived from a *t*-plot. The BJH desorption cumulative volume of pores between 2 nm and 300 nm in diameter was found to be 0.27±0.01 cm^3 g^{-1} that is practically equal to the value of 0.267 cm^3 g^{-1} estimated by the HK method at a relative pressure, p/p_0, of 0.989.

Deposition of cadmium sulfide onto the surface of zinc oxide results in an appreciable change of the adsorption/desorption isotherm shape (Fig. 2a), signaling about a considerable decrease in the pore volume and the surface area. In particular, after 30 SILAR cycles of CdS deposition the BET surface area is reduced by almost 3 times – to 38±3 m^2 g^{-1}, while the BJH desorption cumulative surface area is lowered down to 43±3 m^2 g^{-1}. The BJH desorption cumulative volume of pores between 1.7 nm and 300 nm in diameter is also reduced to 0.17±0.01 cm^3 g^{-1}; the value of 0.173 cm^3 g^{-1} is determined by the HK method at a relative pressure of 0.989. Simultaneously, a decrease in the *t*-plot micropore area from 12.4 to 3.7 m^2 g^{-1} is observed.

Figure 2c shows that the deposition of CdS also results in a shift of the pore size distribution peak in the range of 15–90 nm. The pore volume associated with the smallest mesopores as well as the amplitude of the peak at 2−3 nm are also reduced (Fig. 2b).

The electron diffraction pattern of the electrodeposited ZnO reveals a set of distinct rings corresponding to the hexagonal zinc oxide (Fig. 3). The interplane distances of 0.280 nm, 0.246 nm, 0.191 nm, 0.162 nm, and 0.147 nm, derived from the sizes of rings 1−5, can be assigned to the ZnO plane families (100), (101), (102), (110), and (103). The hexagonal structure of the electrodeposited zinc oxide is also supported by the results of the XRD analysis (Fig. 4).

As compared with ZnO samples electron diffraction patterns of ZnO/CdS ones reveal an additional diffuse ring, the inner, medium and outer diameters of which roughly correspond to the interplane distances of 0.34 nm, 0.33 nm, and 0.32 nm (Fig. 3a). This ring can therefore be assigned

7

both to the electron diffraction on the plane families (100), (002), and (101) of hexagonal cadmium sulfide and to the diffraction on the plane family (111) of cubic CdS. However, the analysis of the HRTEM images of the ZnO/CdS film with 30 SILAR cycles speaks in favor of the deposition of hexagonal CdS phase (Fig. 3c). The interplane distance (0.316 nm) that can be observed on the image belongs to the plane family (101) of hexagonal CdS, while no such lattice parameter can be found within the scope of plane families typical for zinc oxide or cubic CdS.

The XRD pattern of the ZnO/CdS film produced after 30 SILAR cycles shows a small peak at $2\Theta = 25–30°$ (Fig. 4, curve 1) belonging to cadmium sulfide, while the rest of reflections originate from the zinc oxide substrate. A large spectral width of the peak caused probably by lattice disorder or/and a small volume of the coherent scattering domains in the CdS deposit as well as a low intensity of the signal prohibit unambiguous determination of the lattice type from the XRD data. However, at the SILAR cycle number as large as 300, when a more substantial amount of CdS is deposited onto the zinc oxide surface, a proper diffraction pattern can be registered (Fig. 4, curve 2) that can be used for CdS phase identification. Analysis of the diffractogram have revealed the existence of hexagonal CdS deposit although the presence of cubic CdS phase is also not excluded.

Apparently, the hexagonal lattice of zinc oxide serves as a crystallographic precondition for hexagonal CdS formation on early stages of deposition. The appearance of cubic CdS at large N probably can be explained taking into account the results of [19]. According to [19], the microstructure of the chemical-bath-deposited CdS films is determined by the deposition mechanism. It has been established that the growth of the film occurs either by ion-by-ion condensation of Cd^{2+} and $S^{2–}$ ions or by adsorption of colloidal CdS NPs formed in the solution, depending on the deposition parameters. The former mechanism of growth results in thin hard adherent and mirror-like reflecting films, whereas the latter one yields thick flaky and diffusely reflecting films. Occurrence of different polymorphic phases of CdS (hexagonal and cubic) has been observed under different growth conditions [19]. The hexagonal polymorph is formed if successive ionic adsorption of cations and anions on the substrate is achieved (that is the case of the

8

SILAR procedure), while predominantly cubic CdS is deposited when CdS nuclei are formed in solution. The above consideration shows that the polymorphism of CdS deposits produced by SILAR can arise from a combined nuclei formation either on the substrate surface as a result of ions adsorption or in the adjacent solution. Therefore, to avoid the latter nucleation process the substrate should be carefully rinsed with a solvent after each immersion. However, such rinsing becomes especially difficult in the case of mesoporous substrates and nanoobjects with a complex spatial configuration (nanotubes, nanorods, nanoplatelets, etc.) that can lead to formation of the cubic CdS due to a direct exchange chemical interaction between the cadmium salt and sodium sulphide dissolved in a liquid phase occluded in the growing CdS deposit.

3.2. Raman characterization of CdS nanoparticles on ZnO substrate.

Recently, we have successfully applied the Raman spectroscopy to characterize CdS NPs deposited onto the ZnO films at low-to-medium number of SILAR cycles [14]. Here we analyze evolution of the Raman spectra of ZnO/CdS heterostructures produced by SILAR at a large cycle number, $N > 30$.

In the studied range of the Raman shifts ($165 - 1000\ \text{cm}^{-1}$) the ZnO/CdS heterostructures produced at $N \geq 10$ exhibit a peak at $300\ \text{cm}^{-1}$ originating from the scattering on the CdS LO phonons [20] as well as two overtones at ~$600\ \text{cm}^{-1}$ and ~$900\ \text{cm}^{-1}$ (Fig. 5). At $N \geq 100$ a low-intensity photoluminescence background becomes detectable as a broad band with a maximum at around 2.4 eV and a spectral width of ~0.2 eV (Fig. 5, inset). The rise of the photoluminescence band indicates a lower contribution of the non-radiative recombination processes at the ZnO/CdS boundaries when increasing the N.

As discussed in [14], at low N the CdS LO band peak is shifted to higher Raman shifts as compared with the bulk cadmium sulfide, most probably due to compressive stress in CdS NPs. Large values of CdS LO band FWHM at low N are determined by essential impact of surface on the phonon scattering in small nanoparticles, as well as an enhanced influence of anharmonicity of

9

atomic oscillations on phonon decay in the deformed CdS lattice. At $N \geq 100$ the LO band position was found to be almost independent of the SILAR cycle number (Table 1). Therewith, the spectral parameters influenced by disorder in CdS NPs, i.e. a width of LO band and an intensity ratio of the SO band to LO band, vary only slightly with increasing the cycle number at $N \geq 100$. This observation is in accordance with the preservation of small size of coherent X-ray scattering domains at large N as well as with constancy of the Urbach energy in a broad N range (see discussion below).

3.3. Photoelectrochemical properties of CdS NPs on ZnO substrate.

The IPCE spectra of the ZnO/CdS electrodes are shown in Fig. 6a. The nature of photocurrent being observed is caused by photogeneration of charge carriers in CdS NPs under the incident light followed by transfer of photoelectrons into ZnO and external circuit onwards and oxidation of electrolyte redox species by photoholes. Sulfite SO_3^{2-} ions in the electrolyte act as a good hole scavenger providing photoholes trapping from CdS NPs which results in a fast photocurrent response whereas S^{2-} ions among other things reduce the solubility of CdS and facilitate its reprecipitation during the photocorrosion process. No more than 5% degradation of photocurrent was observed during the 30 minutes of photoelectrochemical measurements. Efficient spatial separation of photoexcited charge carriers requires CdS energy levels' to lie higher compared to ZnO conduction band edge (E_c) (Fig. 7).

Several distinct features of the photoelectrochemical behavior of the ZnO/CdS heterostructures should be noted. First, the samples exhibit a remarkably high IPCE (*Y)* in the range of CdS fundamental absorption (80 – 90 % for *N* varying from 20 to 60). The most probable reasons for high *Y* values are a close contact between the SILAR-deposited CdS nanoparticles and the ZnO substrate as well as a high density of CdS NPs on the surface of zinc oxide. Lack of a layer of surfactant molecules on CdS NPs surface, which is typically formed when NPs are synthesized separately in colloidal solutions, also contributes to a high rate of electron transfer between the

sensitizer (CdS) and the oxide. At the same time, a large surface area of ZnO/CdS microplatelets contacting with the solution favours to efficient capture of the photogenerated holes by electrolyte components.

Second, a distinct red shift of the long-wavelength edge of photosensitivity with increasing the SILAR cycle number is observed. The corresponding band gaps E_g of the cadmium sulfide in the ZnO/CdS heterostructures were determined by extrapolating the $(Y \times hv)^2 - hv$ dependences to the abscissa axis (Fig. 6b). Table 2 illustrates the relationship between E_g and the SILAR cycle number.

The E_g values in the range from 2.79 to 2.56 eV at $N = 5$–10 are higher than the band gap of bulk cadmium sulfide due to the quantum confinement effect for CdS NPs. The quantum confinement effect for CdS at a small number of SILAR deposition cycles has been observed many times [21, 22]. Particularly, the paper [21] revealed that the increase of N from 3 to 9 is accompanied by the increase of the average CdS particle size from 2.7 nm to 4.7 nm which resulted in the decrease of E_g from 2.65 to 2.47 eV. However, at $N \geq 20$ the band gap decreases and becomes even lower than the value (2.4 eV) typical for bulk CdS. The lowest E_g of 2.27 eV was observed for the case of $N = 200$. The structural characterization of CdS nanoparticles discussed in the previous sections have shown unambiguously the existence of hexagonal CdS forming at early stages of the SILAR albeit the co-existence of cubic CdS at late deposition stages also can not be excluded. It's a common knowledge that polymorphous modifications of CdS are characterised by different band gap values [23-27]. Thus it is possible that polymorphic transitions of CdS observed with the increase of N can give a certain impact on bang gap value variation. Nevertheless it can not be the reason of E_g lowering with the increase of N because the cubic CdS band gap of 2,4 eV exceeds the E_g values derived in current research work.

In paper [13] it was argued that the red shift is not due to a change in bandgap of the CdS layer but rather to a pronounced sub-bandgap tailing, which is amplified by the high surface area in the composite CdS/ZnO film heterostructure. Our current research work shows that along with the

11

fundamental absorption responsible for the linear part of the $(Yh\nu)^2$–$h\nu$ dependences, the exponential dependence of Y on the quantum energy can be observed in the long-wavelength range of the spectra (Fig. 6c). This absorption, as well as fundamental absorption, causes photogeneration of holes and electrons with further transfer of photoelectrons in ZnO conduction band (Fig. 7). Anodic photocurrent generated by ZnO/CdS heterostructure in such process hereinafter is denoted as sub-band-gap (SBG) photoelectrochemical process.

Assuming proportionality between IPCE (Y) and absorption coefficient α, the exponential tail of the Y spectrum indicates that the edge of the absorption spectrum of CdS NPs obeys the Urbach law [26]:

$$\alpha = \alpha_0 \cdot \exp((h\nu - E_g)/E_u) \tag{1}$$

where α_0 is a constant, E_U is the Urbach energy that reflects structural disorder and defectness of a semiconductor.

The electrodeposited zinc oxide exhibits E_U = 196 meV (Table 2) that exceeds the range reported for the nanocrystalline ZnO films produced by different methods (sol-gel spin coating, chemical vapour deposition, etc.): 53–73 meV [29, 30], 100 meV [31], 85–120 meV [32], 90−100 meV [33]. The large Urbach energy evaluated in the present work indicates a high structural and energy inhomogeneity of the electrodeposited ZnO films and correlates with their mesoporous structure.

Table 2 summarizes the Urbach energies estimated from tangents of the linear sections of the ln$Y$ – $h\nu$ dependences for CdS deposited at different N values. E_U decreases from 93 to 67 meV with the increase of N from 5 to 20 and remains almost constant at higher SILAR cycle numbers (N = 20−300). The Urbach energy is as low as 10−20 meV for CdS single crystals with a low defect density, while by an order of magnitude higher E_U values are typically reported for structurally-disordered polycrystalline samples [34]. Relatively high E_U values reported in the present work attest to a high level of structural disorder of CdS NPs produced by SILAR, confirming the results of the Raman spectroscopy discussed earlier in the section 3.2 and in [14]. It can be assumed that at

a constant E_U (in the range of $N = 20$–300) the density of electronic states and their energy distribution in the band gap of CdS NPs remain also identical. As no increase in the defect density and disorder takes place in CdS NPs as the N grows, these factors cannot contribute to the red shift of the long-wavelength edge of the photocurrent spectra.

Figure 8 shows the dependences of IPCE (Y) of the ZnO/CdS electrodes on the N for different monochromatic excitation wavelengths. The Y at $\lambda = 400$ nm (3.10 eV) grows as the N increases from 5 to 60 and then decreases considerably at higher number of the SILAR cycles (Fig. 8, curve 1). The photocurrent growth in the range of N from 5 to 60 is an obvious result of the increase in the CdS layer absorbance. A decrease of Y at $N > 60$ can be explained by enhanced recombination losses in CdS as a result of expansion of the distance between the charge carrier generation area and ZnO substrate [22]. The latter assumption is strongly supported by the effect of CdS photoluminescence enhancement observed experimentally with the increase of N (Fig. 5).

Under illumination with monochromatic green ($\lambda = 530$ nm) and red ($\lambda = 625$ nm) light photocurrent increases in a much broader SILAR cycle number range – till $N = 100$ and only at higher N a decrease of photocurrent is observed (Fig. 8, curves 2 and 3). As it will be shown below, the illumination of CdS by red and green light results exclusively in a sub-band-gap photoelectrochemical activity. CdS NPs have a small absorption coefficient below the band gap and therefore SBG absorbance increases without saturation in a much broader N range (till $N = 100$) as the thickness of the CdS layer increases. However, in the case of comparatively thick sensitizer layers ($N > 100$) the photocurrent generation efficiency is also limited by the recombination losses on the inter-crystallite interfaces.

To shed more light on difference between the band-gap and sub-band-gap photoelectrochemical processes in ZnO/CdS heterostructures, we have analyzed photocurrent - potential curves registered under monochromatic illumination of the ZnO/CdS electrodes (Fig. 9). The experiments were focused on the ZnO/CdS samples with large SILAR cycle number ($N = 300$)

13

as such samples exhibit pronounced shift of red threshold of photoelectrochemical activity with respect to the band gap of bulk CdS.

The onset potential of the ZnO/CdS electrodes illuminated by comparatively high-energy quanta (λ = 400 nm; $h\nu$ = 3.10 eV) is observed at E_{on} = –900 mV. When electrode is illuminated by a lower-energy light flux − green (λ = 530 nm; $h\nu$ = 2.34 eV) and red (λ = 625 nm; $h\nu$ = 1.98 eV), the onset potential is shifted to the less negative values of E = –850 mV and –800 mV, respectively. The E_{on} value can be used for determination of the band edge positions of semiconductor electrodes (in particular, the conduction band bottom for n-type semiconductors) [35]. Illumination of CdS NPs with the quanta larger than the band gap ($h\nu \geq E_g$) results in interband electron transitions. In this case E_{on} = –900 mV can be adopted as an approximate conduction band edge (E_c) expressed in terms of the electrode potential scale. On the other hand, illumination of CdS NPs with $h\nu$ = 1.98 eV (red light) can't initiate the interband electron transitions. Obviously, in this case photoelectrochemical processes go on with the participation of the charge carriers generated in the defect states tailing into the band gap (Fig. 7). It can be concluded, therefore, that the electron states in the band gap have more positive electrode potentials (up to 100 mV) than the conduction band edge. Noteworthy the illumination of the ZnO/CdS electrodes by green light with λ = 530 nm (2.34 eV) also shifts the onset potential (for 50 mV, as compared to E_c) despite the fact that the excitation energy in this case exceeds the derived CdS E_g value (2.30 eV). The nature of this fact is explained below.

In paper [13] it was argued, that optical effects due to light scattering may be important in explaining the red-shifted spectrum. Scattering in a totally nonabsorbing film will not lead to any absorption, but it can only increase an already existing absorption in sub-band gap tailing. Such absorption in a transparent film was essentially not noticeable and becomes much stronger in the scattering one. When E_g is derived from the photocurrent spectra, it is assumed that the photocurrent is directly proportional to the number of absorbed photons in the analyzed wavelength

range. A portion η_{abs} of the absorbed quanta from the light flux travelling through a medium containing k absorbing particles can be expressed as

$$\eta_{abs} = 1 - \exp(-Ak), \qquad (2)$$

where A is the optical density of a single absorbing particle. It is obvious that the scattering can affect the photocurrent spectra by increasing the apparent number k in equation (2).

Within the scope of fundamental absorption for direct transitions eq. (2) can be expressed as

$$\eta_{abs} = 1 - \exp(-C(hv-Eg)^{1/2}d \cdot k/hv), \qquad (3)$$

where d is the particle size, C is a constant independent of the quantum energy [36]. The C constant can be estimated using the reported in [37] transmission spectra of CdS/In$_2$O$_3$ films (where CdS NPs were grown by SILAR) with a thickness of around 40 nm that is much smaller than both the thickness of the present ZnO/CdS films and the excitation wavelengths. Assuming $C \approx 2 \times 10^7$ m^{-1} eV$^{1/2}$, $d = 10^{-8}$ m, and $E_g = 2.4$ eV, a function $\eta_{abs}(hv)$ can be plotted in the Tauc coordinates for different k values (Fig. 10).

Figure 10 demonstrates that sublinearity of the $(\eta_{abs} \cdot hv)^2 - hv$ dependence is negligible in the range of small k and the E_g value, derived by a linear approximation, is close to 2.4 eV. However, as the k grows, the sublinearity of the $(\eta_{abs} \cdot hv)^2 - hv$ curves increases, resulting in the E_g values smaller than 2.4 eV. It should be noted that the films reported in [37] exhibited low light scattering efficiency and the band gap of CdS NPs of the largest size reported (at $N = 50$), $E_g = 2.42$ eV, was very close to the conventional band gap of bulk cadmium sulfide.

Hence, the effect of multiple light scattering can result in *lowered apparent E_g values* derived from the parabolic dependences typical for the direct electron transitions. In this view, the band gap estimated from the photocurrent spectra by such methodology should be considered as an effective value shifted to lower energies owing to the multiple light scattering.

4. Conclusions.

Cadmium sulfide nanoparticles deposited by the SILAR method on the surface of the mesoporous ZnO microplatelets with a high surface area (110 ± 10 m^2 g^{-1}) are responsible for two types of photoelectrochemical processes induced by the band-gap (BG) and sub-band-gap (SBG) photoexcitation. The both types are characterized by a high incident photon-to-current conversion efficiencies (Y) with maximum values reaching 90 % for BG processes and 25 % for SBG ones. High Y values originate from an intimate contact between CdS NPs and zinc oxide substrate, as well as a large surface area of ZnO/CdS photoanode. While in the BG processes the visible-light sensitization of photoelectrochemical activity arises from the injection of the photogenerated electrons into the conduction band of CdS, the SBG photoelectrochemical processes involve the charge transfer with the participation of the electron states in a sub-band-gap tail of the fundamental absorption band. Photocurrent - potential measurements showed that the tail states contributing to the photocurrent generation are located in the band gap of CdS nanoparticles by 0.1 eV lower than the conduction band edge (around 100 mV on the electrode potential scale).

Dependence of the photocurrent density on the sensitizer quantity proportional to the SILAR cycle number is different for the BG and SBG photoelectrochemical processes. In the former case the highest photocurrent is observed at a lower amount of cadmium sulfide. As the BG photoelectrochemical processes are determined by the fundamental light absorption with high absorption coefficients, an increase in the CdS layer thickness results in enhancement of recombination of photogenerated charge carriers transferred through the sensitizer layer to ZnO. On the contrary, the SBG light absorption has a low efficiency, and an increase in the overall light absorbance with increasing the amount of CdS NPs plays a pivotal role in the case of the SGB photoelectrochemical processes.

The Urbach energy (E_U) of CdS NPs as a function of the SILAR cycle number N was determined from the photocurrent spectra. The E_U is maximal at initial deposition stages ($E_U = 93$ mV at $N = 5$), then mildly decreases ($E_U = 73$ mV at $N = 10$) and remains steady in the range of N from 20 to 300 ($E_U = 67\pm1$ mV). A Raman spectroscopy study of the ZnO/CdS

16

heterostructures showed that the spectral width of the LO peak of CdS NPs which reflects the structural disorder in the NPs decreases only slightly and monotonically with increasing the *N*. This fact indicates that the red shift of band edge in the photocurrent spectra of the ZnO/CdS heterostructures with an increase of *N* can't be explained by enhancement of the structural disorder of CdS NPs. The most probable reason of the red shift of the photocurrent spectra with an increase in the SILAR cycle number as well as the high efficiency of SBG photoelectrochemical processes lies in *the light scattering* in the ZnO/CdS films caused by inherent inhomogeneities with the size comparable with wavelengths of the incoming light.

The reported results show that the efficiency of the third-generation solar cells based on mesoporous wide-band-gap metal oxide materials can be enhanced by expansion of the spectral sensitivity range of the photoanodes using the sub-band-gap photoelectrochemical processes that can generate photocurrent with a high quantum yield.

17

Captions for Figures:

Figure 1. SEM images of the ZnO film with low-magnification (a) and high-magnification (b) and ZnO with 300 CdS SILAR cycles (c).

Figure 2. Nitrogen adsorption-desorption isotherms at 77 K (*a*), Horvath-Kawazoe differential pore volume plots (*b*), and BJH pore size distribution derived from the desorption branch of the isotherm (*c*) for ZnO film (*1*) and ZnO/CdS film with 30 CdS SILAR cycles (*2*).

Figure 3. (a) − Selected-area electron diffraction patterns of ZnO (section I) and ZnO with 30 CdS SILAR cycles heterostructure (section II); TEM images of ZnO (b) and ZnO with 30 CdS SILAR cycles (c) microplatelets detached from the FTO surface. HRTEM images on the insets in (b) and (c) depicts the interplane distance of ZnO and CdS respectively.

Figure 4. X-ray diffractograms of the ZnO/CdS films at cycle number $N = 30$ (*1*) and $N = 300$ (*2*).

Figure 5. Raman spectra of the ZnO/CdS films at cycle number $N = 0$ (*1*), 5 (*2*), 10 (*3*), 20 (*4*), 30 (*5*), 50 (*6*), 100 (*7*), 200 (*8*), 300 (*9*). The curves are arranged along the Y-axis for convenience. Inset shows a PL spectrum of the ZnO/CdS film prepared at $N = 300$.

Figure 6. Spectral dependences of the external quantum efficiency Y presented in the coordinates $Y - \lambda$ (*a*), $(Y \times h\nu)^2 - h\nu$ (*b*), and $\ln Y - h\nu$ (*c*). Electrodes: ZnO (*1*) and ZnO/CdS (*2 − 6*) at $N = 5$ (*2*), 10 (*3*), 20 (*4*), 60 (*5*) and 200 (*6*). Electrolyte: 0.1 M Na_2S + 0.1 M Na_2SO_3. E vs. Ag/AgCl/KCl (sat.) = −200 mV. The arrows in Fig. 6a correspond to the band gap values of CdS NPs given in Table 2.

Figure 7. Depiction of band-gap and sub-band-gap photoexcitations considering the defect states tailing into the band gap.

Figure 8. Dependence of *Y* on the SILAR cycle number for the ZnO/CdS heterostructure ($N = 300$) illuminated by monochromatic light with a wavelength of 400 nm (*1*), 530 nm (*2*), 625 nm (*3*). *E* vs. Ag/AgCl/KCl (sat.) $= -300$ mV.

Figure 9. Photocurrent *vs* potential curves for the ZnO/CdS heterostructure produced at $N = 300$ under illumination with monochromatic light. The wavelength is 400 nm (*1*), 530 nm (*2*), 625 nm (*3*).

Figure 10. $(\eta_{abs}h\nu)^2 - h\nu$ plot for $k = 10$ (*1*), $k = 20$ (*2*), $k = 30$ (*3*) and $k = 50$ (*4*); η_{abs} is a fraction of absorbed photons; k is the number of absorbing CdS NPs.

References

[1] Y. Nicolau, Solution deposition of thin solid compound films by a successive ionic-layer adsorption and reaction process, Appl. Surf. Sci. 22 (1985) 1061.

[2] Y. Nicolau, M. Dupuy, M. Brunel, ZnS, CdS, and $Zn_{1-x}Cd_xS$ thin films deposited by the successive ionic layer adsorption and reaction process, J. Electrochem. Soc. 137 (1990) 2915.

[3] Y. Nicolau, J. Menard, Solution growth of ZnS, CdS and $Zn_{1-x}Cd_xS$ thin films by the successive ionic-layer adsorption and reaction process; growth mechanism, J. Crystal Growth 92 (1988) 128.

[4] R. Vogel, P. Hoyer, H. Weller, Quantum-sized PbS, CdS, Ag_2S, Sb_2S_3 and Bi_2S_3 particles as sensitizers for various nanoporous wide-bandgap semiconductors, J. Phys. Chem. 98 (1994) 3183.

[5] H. Pathan, C. Lokhande, Deposition of metal chalcogenide thin films by successive ionic layer adsorption and reaction (SILAR) method, Bull. Mater. Sci. 27 (2004) 85.

[6] T. Kanniainen, S. Lindroos, J. Ihanus, M. Leskela, Growth of lead selenide thin films by the successive ionic layer adsorption and reaction (SILAR) technique, J. Mater. Chem. 6 (1996) 983.

[7] N. Guijarro, T. Lana-Villarreal, T. Lutz, S. Haque, R.Gómez, Sensitization of TiO_2 with PbSe quantum dots by SILAR: how mercaptophenol improves charge separation, J. Phys. Chem. Lett. 3 (2012) 3367.

[8] L. Chong, H. Chien, Y. Lee, Assembly of CdSe onto mesoporous TiO_2 films induced by a self-assembled monolayer for quantum dot-sensitized solar cell applications, J. Pow. Sour. 195 (2010) 5109.

[9] S. Cheng, W. Fu, H. Yang, L. Zhang, J. Ma, H. Zhao, M. Sun, L. Yang, Photoelectrochemical performance of multiple semiconductors (CdS/CdSe/ZnS) cosensitized TiO_2 photoelectrodes, J. Phys. Chem. C. 116 (2012) 2615.

[10] M. Genovese, I. Lightcap, P. Kamat, Sun-believable solar paint. A transformative one-step approach for designing nanocrystalline solar cells, ACS Nano. 6 (2012) 865.

[11] A. Ubale, R. Dhokne, P. Chikhlikar, V. Sangawar, D. Kulkarni, Characterization of nanocrystalline cadmium telluride thin films grown by successive ionic layer adsorption and reaction (SILAR) method, Bull. Mater. Sci. 29 (2006) 165.

[12] D. Baker, P. Kamat, Photosensitization of TiO_2 Nanostructures with CdS quantum dots: particulate versus tubular support architectures, Adv. Funct. Mater. 19 (2009) 805.

[13] E. Rabinovich, G. Hodes, Effective bandgap lowering of CdS deposited by successive ionic layer adsorption and reaction, J. Phys. Chem. C 117 (2013) 1611.

[14] A. Kozitskiy, O. Stroyuk, S. Kuchmiy, A. Mazanik, S. Poznyak, E. Streltsov, A. Kulak, O. Korolik, V. Dzhagan, Photoelectrochemical and Raman characterization of nanocrystalline CdS grown on ZnO by successive ionic layer adsorption and reaction (SILAR) method, Thin Solid Films 562 (2014) 56.

[15] A. Kozytskiy, A. Stroyuk, S. Kuchmiy, M. Skoryk, V. Moskalyuk, Morphology, photochemical, and photocatalytic properties of nanocrystalline zinc oxide films, Theoret. Experim. Chem. 5 (2012) 331.

[16] S. Gregg, K. Sing, Adsorption surface area and porosity, Academic Press, London, 1982.

[17] K. Sing, D. Everett, R. Haul, L. Moscou, R. Pierotti, J. Rouquerol, T. Siemieniewska, Reporting physisorption data for gas/solid systems with special reference to the determination of surface area and porosity, Pure Appl. Chem. 57 (1985) 603.

[18] J. Groen, L. Peffer, J. Perez-Ramirez, Pore size determination in modified micro- and mesoporous materials. Pitfalls and limitations in gas adsorption data analysis, Micropor. Mesopor. Mat. 60 (2003) 1.

[19] I. Kaur, D. Pandya, K. Chopra, Growth kinetics and polymorphism of chemically deposited CdS films, J. Electrochem. Soc.127 (1980) 943.

[20] B. Tell, T. Damen, S. Porto, Raman effect in cadmium sulfide, Phys. Rev. 144 (1966) 771.

[21] R. Ahmed, G. Will, J. Bell, H. Wang, Size-dependent photodegradation of CdS particles deposited onto TiO_2 mesoporous films by SILAR method, J. Nanopart. Res. 14 (2012) 1140.

[22] G. Hodes, Comparison of dye- and semiconductor-sensitized porous nanocrystalline liquid junction solar cells, J. Phys. Chem. C 112 (2008) 17778.

[23] R. Bube, Photoconductivity of Solids, John Wiley and Sons, New York, 1960.

[24] M. Cardona, M. Weinstein, A. Wolff, Ultraviolet reflection spectrum of cubic CdS, Phys. Rev. 140 (1965) A633.

[25] N. Stoffel, Experimental band structure of cadmium sulfide, Phys. Rev. B 28 (1983) 3306.

[26] O. Madelung, Landolt-Börnstein Numerical Data and Functional Relationships in Science and Technology, Verlag, Berlin-Heidelberg-New York, 1982.

[27] M. Weber, Handbook of optical materials, CRC Press, London-New York-Washington, 2003.

[28] F. Urbach, The long-wavelength edge of photographic sensitivity and of the electronic absorption of solids, Phys. Rev. 92 (1953) 1324.

[29] M. Caglar, S. Ilican, Y. Caglar, F. Yakuphanoglu, Electrical conductivity and optical properties of ZnO nanostructured thin film, Appl. Surf. Sci. 255 (2009) 4491.

[30] S. Ilican, Y. Caglar, M. Caglar, Preparation and characterization of ZnO thin films deposited by sol-gel spin coating method, J. Optoelectron. Adv. Mater. 10 (2008) 2578.

[31] N. Shakti, P. Gupta, Structural and optical properties of sol-gel prepared ZnO thin film, Appl. Phys. Res. 2 (2010) 19.

[32] S. Xue, X. Zu, W. Zhou, H. Deng, X. Xiang, L. Zhang, H. Deng, Effects of post-thermal annealing on the optical constants of ZnO thin film, J. Alloy. Compd. 448 (2008) 21.

22

[33] Y. Natsume, H. Sakata, T. Hirayama, Low-temperature electrical conductivity and optical absorption edge of ZnO films prepared by chemical vapour deposition, Phys. Stat. Sol. A 148 (1995) 485.

[34] A. Ziabari, F. Ghodsi, Growth, characterization and studying of sol–gel derived CdS nanocrystalline thin films incorporated in polyethyleneglycol: effects of post-heat treatment Sol. Energ. Mat. Sol. C. 105 (2012) 249.

[35] G. Redmond, A. O'Keeffe, C. Burgess, C. MacHale, D. Fitzmaurice, Spectroscopic determination of the flatband potential of transparent nanocrystalline zinc oxide films, J. Phys. Chem. 97 (1993) 11081.

[36] R. Smith, Semiconductors, Cambridge University Press, Cambridge, 1978.

[37] M. Malashchonak, S. Poznyak, E. Streltsov, A. Kulak, O. Korolik, A. Mazanik, Photoelectrochemical and Raman characterization of In_2O_3 mesoporous films sensitized by CdS nanoparticles, Beilstein J. Nanotechnol. 4 (2013) 255.
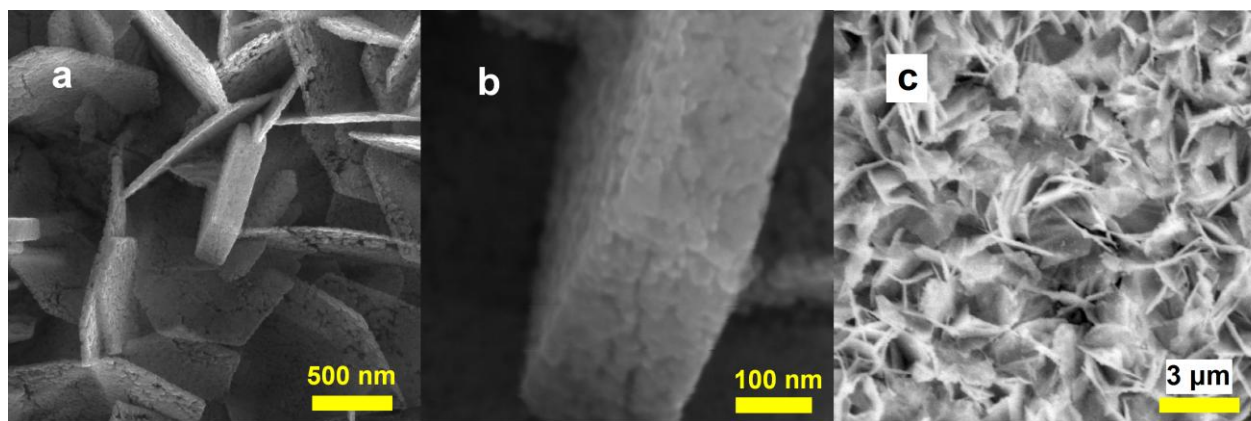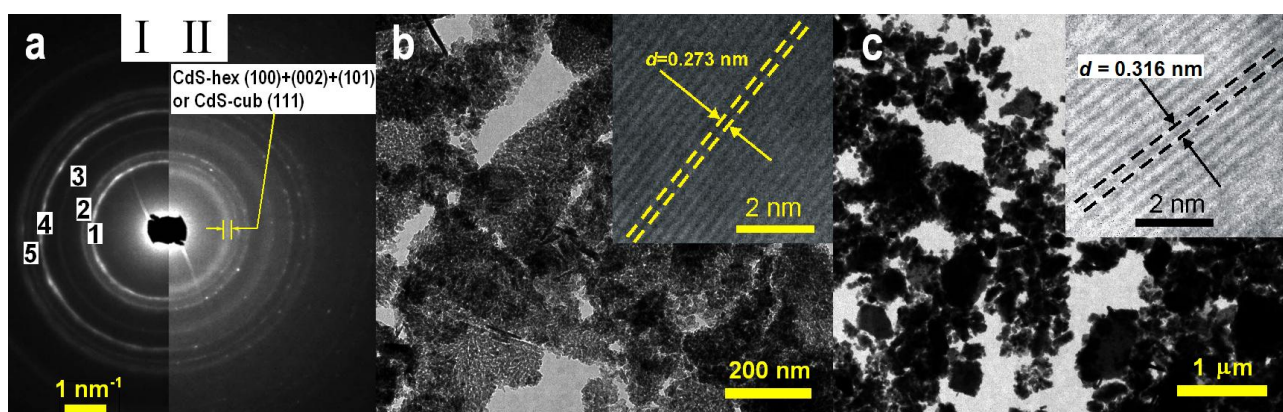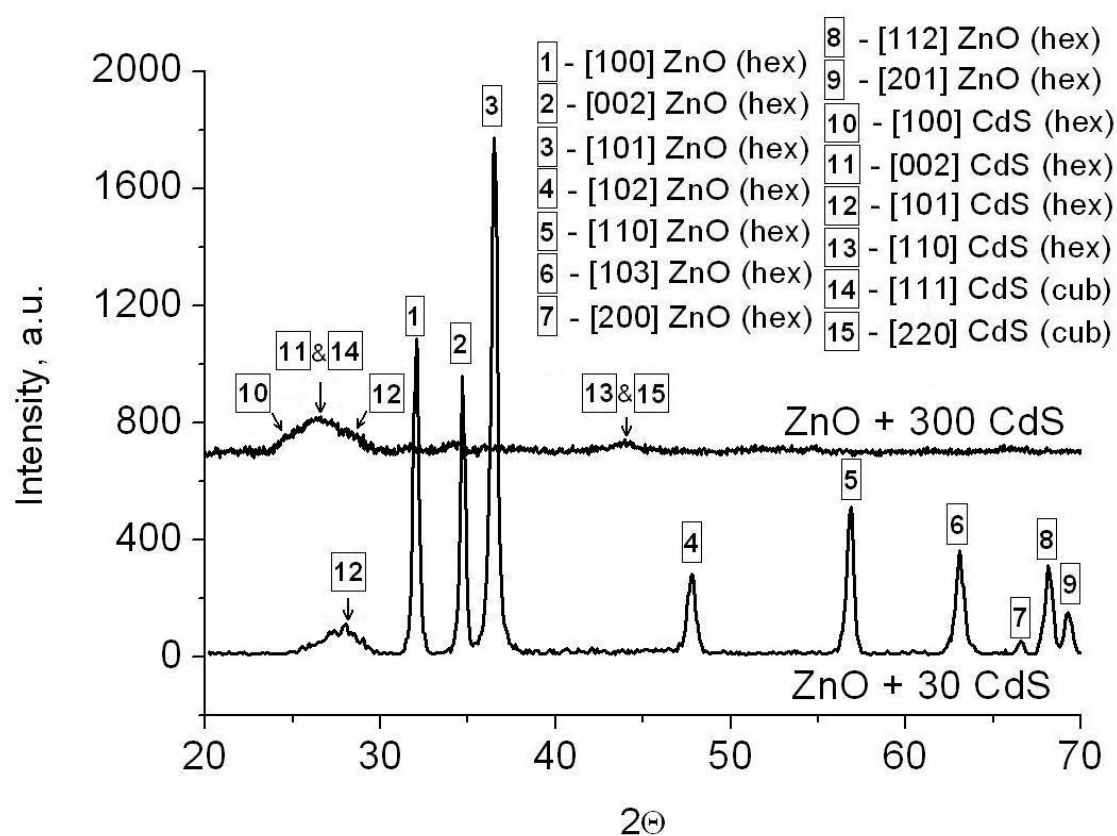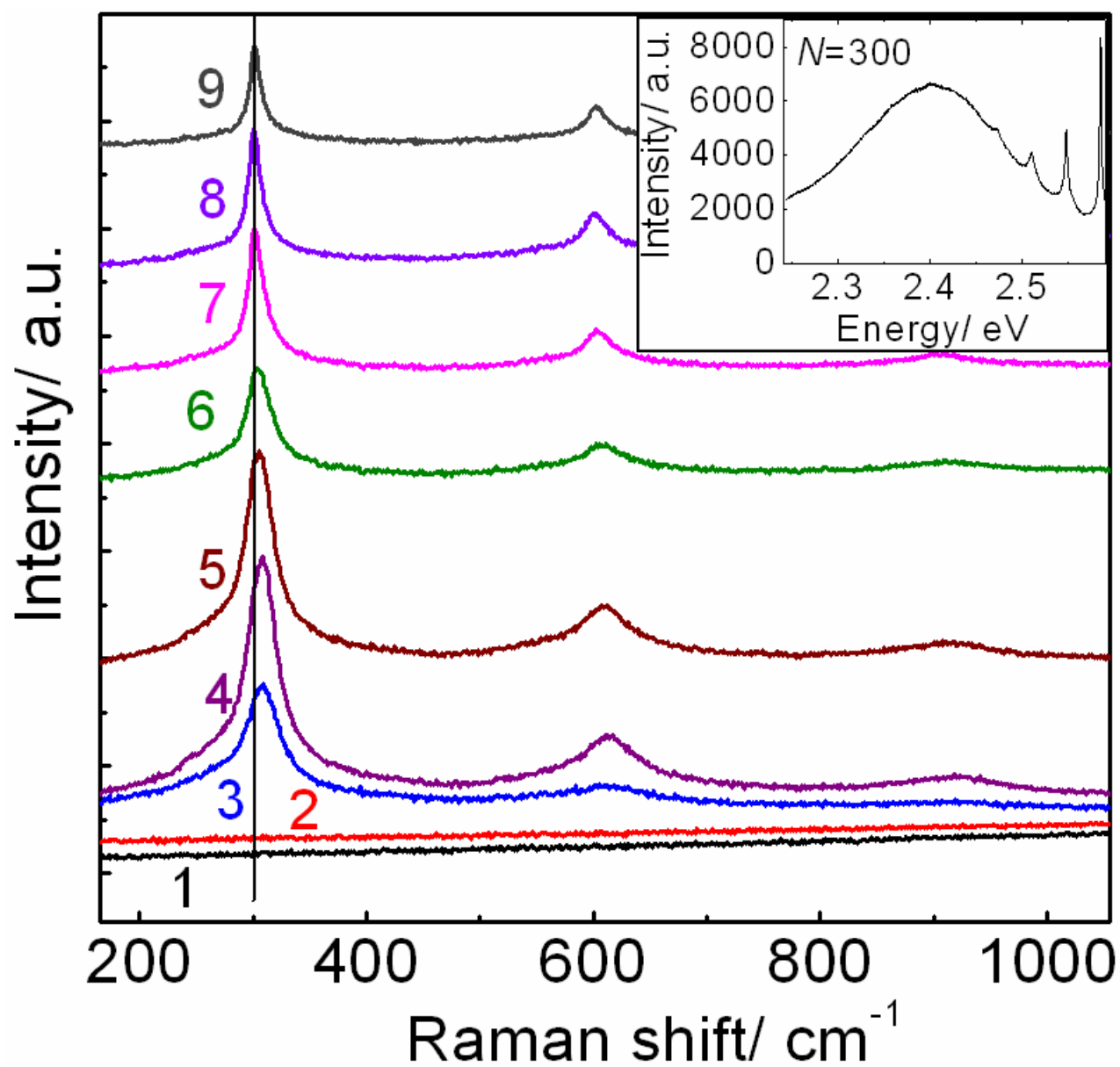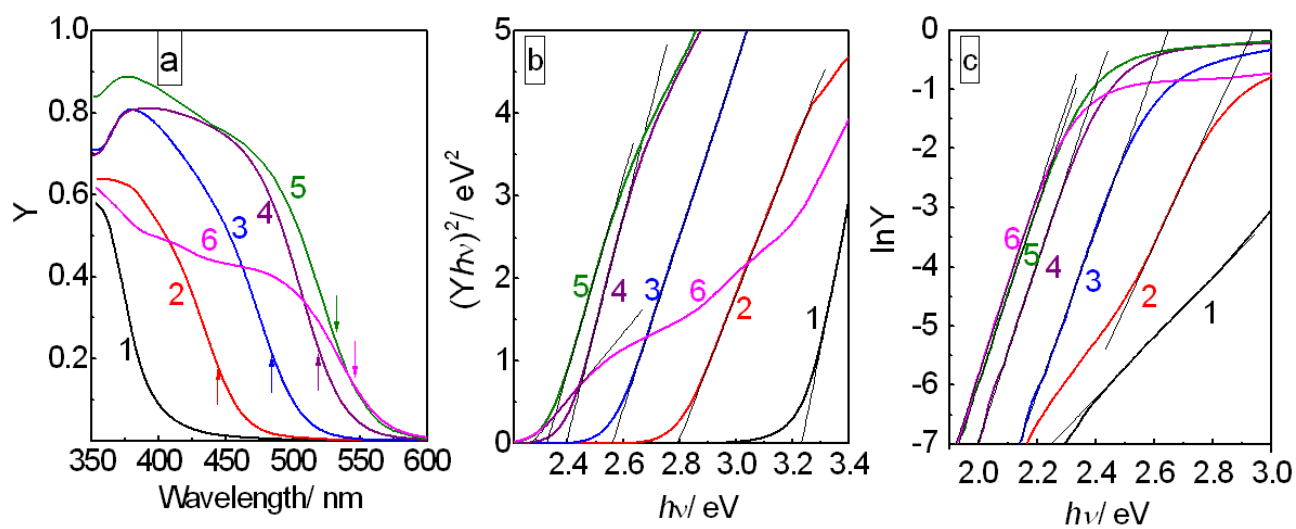
Figure 1
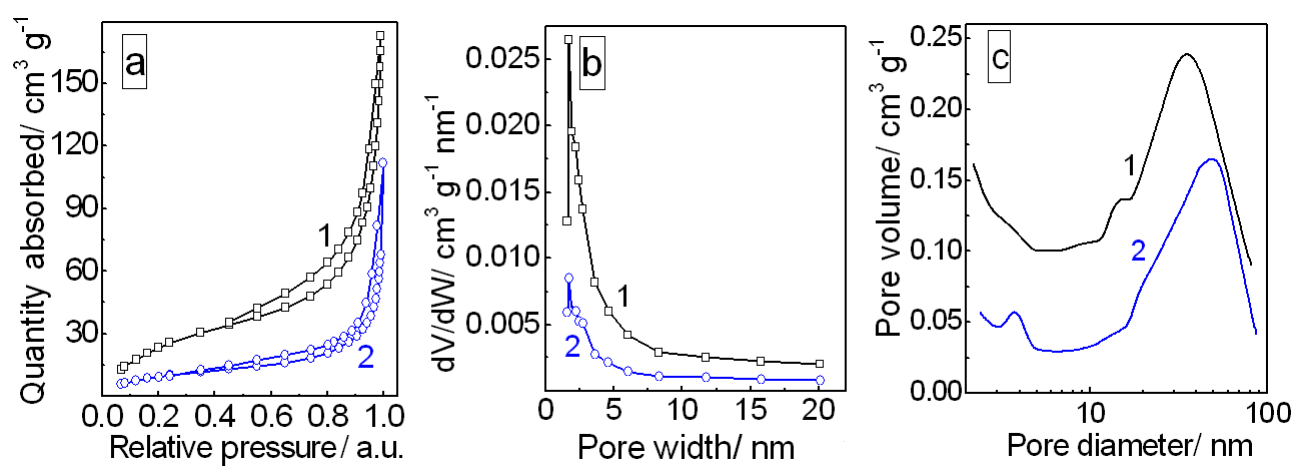
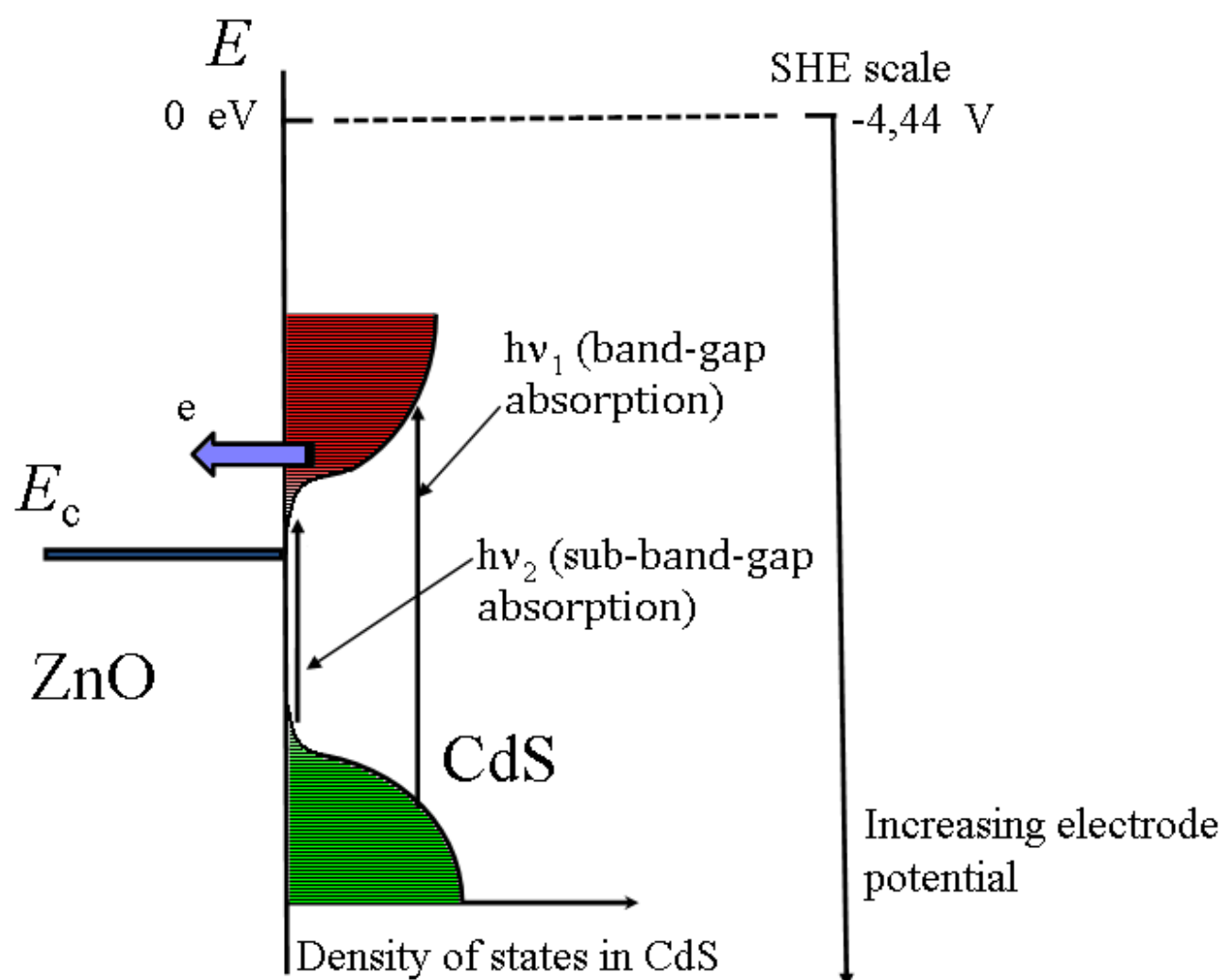Figure 2

Figure 3

Figure 4

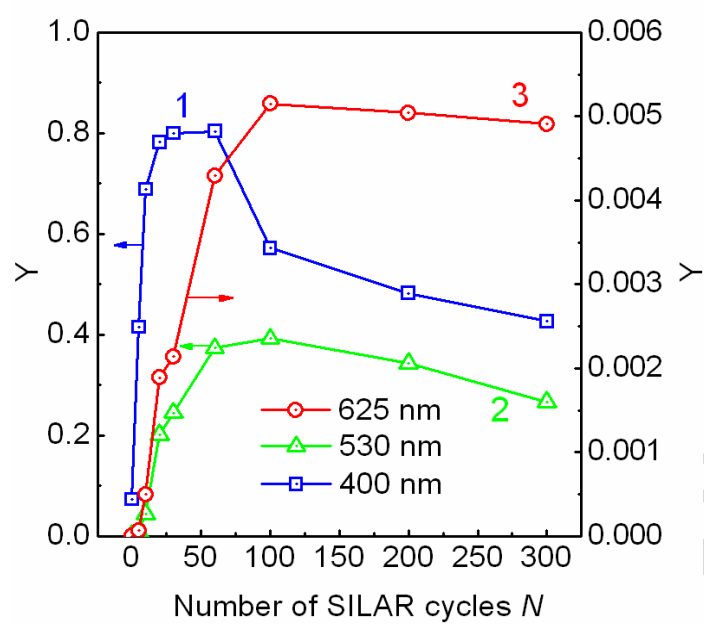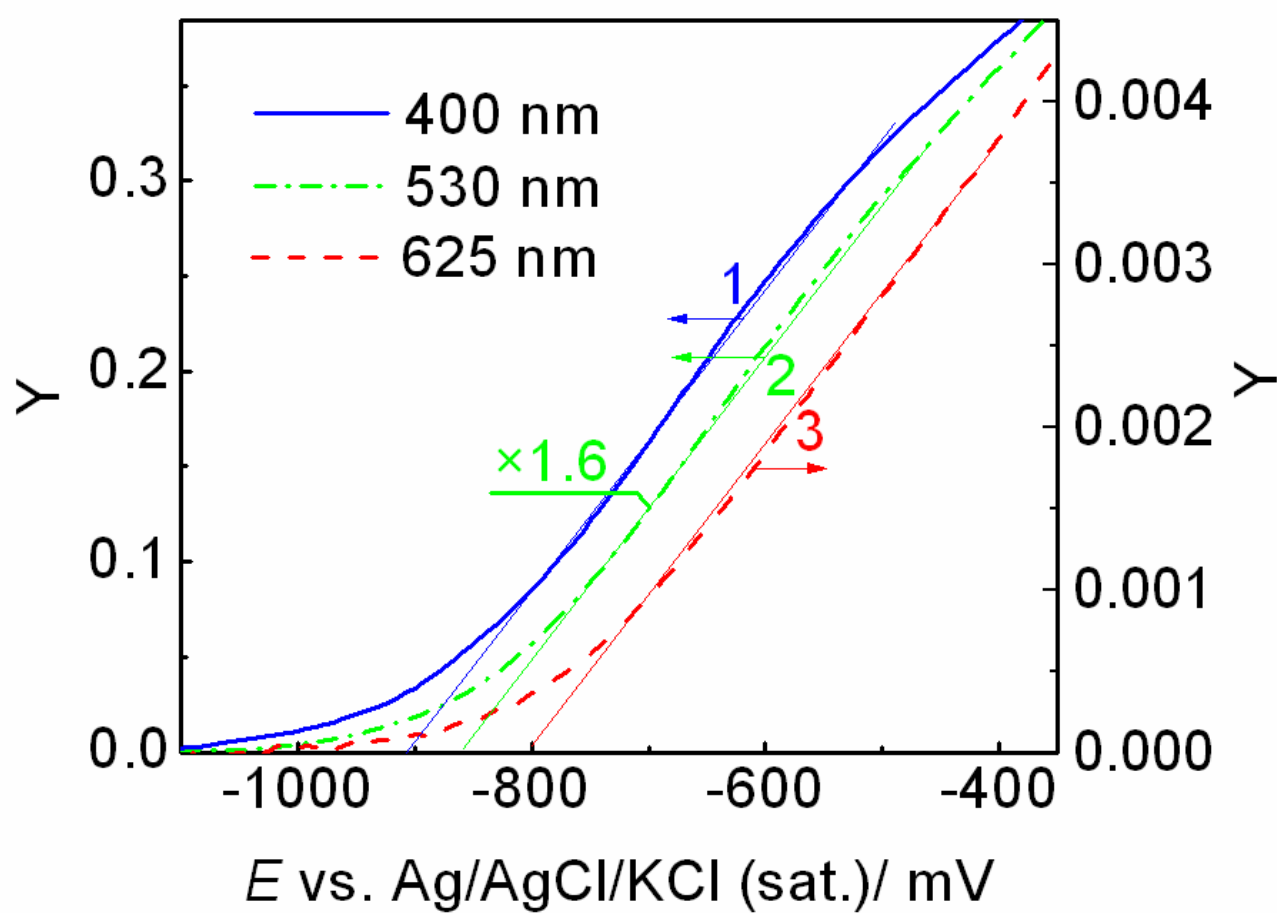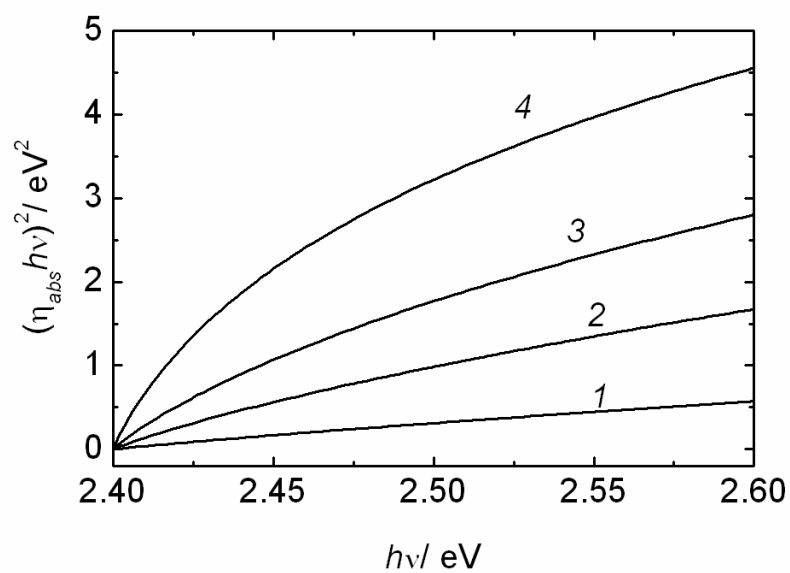Figure 5

Figure 6

Figure 7

Figure 8

Figure 9

Figure 10

Table 1. CdS LO band position and full width on the half-maximum in Raman spectra for the ZnO/CdS films prepared at different SILAR cycles number N.

N	CdS LO peak position/ cm^{-1}	CdS LO peak FWHM/ cm^{-1}
10	308.4	36
20	307.8	32
30	305.7	30
50	305.0	29
100	302.0	21
200	301.3	17
300	301.6	15

Table 2. Direct band gap E_g and Urbach energy E_U for the ZnO and ZnO/CdS films prepared at different SILAR cycles number N.

N	E_g/ eV	Linearity range for E_g determination/ eV	E_U/ meV	Linearity range for E_U determination/ eV
0	3.23±0.01	3.30÷3.43	196±2	2.46÷2.86
5	2.79±0.01	2.87÷3.24	93±1	2.56÷2.73
10	2.56±0.01	2.65÷3.14	73±1	2.13÷2.46
20	2.39±0.01	2.46÷2.60	67±1	1.97÷2.27
30	2.38±0.01	2.45÷2.57	67±1	1.92÷2.25
60	2.33±0.01	2.4÷2.54	67±1	1,97÷2.21
100	2.29±0.01	2.36÷2.46	67±1	1.88÷2.18
200	2.27±0.01	2.34÷2.44	66±1	1.92÷2.17
300	2.30±0.01	2.38÷2.52	68±1	1.94÷2.14

Highlights

ZnO/CdS films demonstrate high quantum efficiency (25%) for sub-band-gap transitions.

Onset photocurrent potentials for sub-band-gap processes differ than those for band-gap ones.

Sub-band-gap transitions are caused by band-tail states in CdS nanoparticles.